JOURNAL OF MATERIALS SCIENCE 12 (1977) 1253–1271

Liquid drop collisions on deformable media

WILLIAM F. ADLER
Effects Technology, Inc, 5383 Hollister Avenue, Santa Barbara, California, USA

The spatial and temporal distributions of the transient stresses generated in elastically deformable bodies with the elastic properties of zinc selenide, polymethylmethacrylate, and soda-lime glass have been evaluated for an idealized representation of a water drop impacting a plane surface. The development of regions of significant tensile stresses within the target material is clearly shown which can be related to fracture initiation in brittle materials. The analytical approach used has its inherent shortcomings which include the lack of obtaining the stresses at the surface in the vicinity of the Rayleigh wave front and the fact that it is only applicable to the earliest stages of the impact event before lateral outflow dominates. However, the idealized model reasonably approximates the results from numerical analyses with regard to the water drop shape profile in the initial stage of the impact when the compressibility of the water in the drop is most significant. It does appear that the period of the collision covered by the analysis is where the damage within the material originates, whether due to the deformations within the impact zone or by the transient stress distribution established after the passage of the shear wave into the target material.

1. Introduction

The analysis of liquid drop impingement presented here is specialized to the experimental conditions associated with a research programme on the erosion of transparent materials. In order to investigate the effects of multiple water drop impacts, the target materials are exposed to a simulated rainfield in the AFML/Bell and AFML rotating arm facilities.* The rainfield in these facilities has been standardized to a 2.54 cm h^{-1} rainfall of 1.8 mm diameter water drops. Most plastics and glasses cannot withstand exposures to this environment for more than a few minutes at impact velocities between 222 to 314 m sec^{-1} (500 to 700 mph) before erosion of the exposed surface is evident. In some circumstances the utility of transparent materials is degraded at exposure times prior to when a measureable mass loss is recorded. This fact motivated a more careful examination of the damage initiated on a material surface by collision with a single water drop at subsonic velocities.

Detailed knowledge of the flow patterns and impact pressures developed during the collision of a liquid drop and a deformable plane surface is still unavailable. The qualitative details of a liquid drop impact have been obtained from a number of high-speed photographic studies [1–6]. The experimental data for spherical drops striking a solid surface still cannot provide a quantitative description of the temporal magnitude and distribution of the liquid/solid interfacial pressure; however, direct pressure measurements over a very small region of the contact area of an impacting drop [6–10] are beginning to supply the required information.

An estimate of the events which take place when a liquid drop strikes a plane surface will be reviewed as they are described in the literature and from the damage seen in our own experiments on the erosion of materials. This information is used in conjunction with a simple model of the drop collision to obtain quantitative evaluations of the transient stress states in the target material. Know-

---

* The AFML/Bell rotating arm is located at Bell Aerospace Co, Wheatfield, New York; the AFML rotating arm is located at Wright-Patterson Air Force Base, Ohio, USA.

© *1977 Chapman and Hall Ltd. Printed in Great Britain.*

ing the dynamic stress conditions the target experiences can be useful in describing the mode of initial failure. The role of the impact loadings and the response of the material target to these loadings have not been clearly defined in the erosion literature. While all the details of the liquid drop collision are not included in the present approach, the general response of the target is certainly clearly defined. The analysis has been carried out for three materials which represent a moderately broad range of elastic properties: soda-lime glass, polymethymethacrylate (PMMA), and zinc selenide (ZnSe).

2. Collision of a liquid drop with a plane surface

The initial damage produced on solid surfaces due to liquid drop impingement arises from two sources: the direct pressure generated over the expanding impact area in order to bring the drop to a sudden stop and the high-velocity lateral outflow of the liquid subsequently escaping from the high pressure zone. In general little agreement can be found in the literature concerning the analysis of the sequence of events which takes place at a solid surface impacted by a liquid drop.

When a liquid drop first strikes a plane surface, the boundary of the contact area will be travelling at supersonic speeds with respect to the dilatational wave speed for the impacted body. For a homogeneous and isotropic elastic material, the period of time for which the radial velocity of the contact zone exceeds the dilatational wave speed will depend on the radius and initial impact velocity of the liquid drop and the compressibility of the elastic material. The time-dependent radius of the contact area during the collision of a completely compressible liquid drop with a rigid surface is given by

$$a(t) = \sqrt{[2RV_0t-(V_0t)^2]} \qquad (1)$$

where V_0 is the impact velocity, R is the radius of the spherical drop, and t is the time elapsed from the initial contact.

Analyses have been developed for evaluating the pressure applied to a rigid surface due to an impacting liquid drop or cylindrical liquid slug. Huang [11], in particular, has presented the most complete fluid mechanics analysis with computer solutions to indicate the temporal and spatial evolution of the impact pressure and lateral outflow at impact velocities of 300 and 746 m sec^{-1}. Recently, Hwang [12] extended Huang's finite difference computations for the collision of a liquid drop with an elastic half-space; however, the evaluations of the transient stress states within the half-space exhibited a fair degree of irregularity. In carrying out these computations, Hwang modified Huang's boundary conditions for a liquid drop striking a rigid surface. Hwang viewed this case as two drops colliding with equal but opposite velocity, instead of assuming that the velocity component normal to the plane surface was zero, as Huang did. This alternative view and a slight difference in the conditions along the axis of symmetry produced a significant difference in the computed pressure distribution. These computations neglect the viscosity and surface tension of the liquid and are based on Tait's equation of state for water. The inertia effects and compressibility of the impacting water drop are taken to be the dominant features in these computations.

Computations for a water drop striking a deformable half-space at velocities up to 342 m sec^{-1} are currently being carried out by Kreyenhagen *et al.* [13] who employ the Walker–Sternberg equation of state for water. Again, discrepancies with the previous finite difference schemes are observed in the pressure distributions and drop profiles which will be described subsequently.

Huang's calculations support Engel's contention [14] that the pressure build-up and lateral outflow occur simultaneously after the initial contact is made, although the jetting is not appreciable during the early stage of impact. This contradicts the opinions of Morris [15], Heymann [16], and Bowden and Field [3] that lateral flow cannot begin before the compression wave in the fluid moves ahead of the circular boundary between the drop and the solid surface. At approximately 100 m sec^{-1} these calculations indicate that the critical edge angle is on the order of a few degrees. Brunton and Camus [5], however, provide photographic evidence that under these conditions, the critical angle, ϕ, falls in the range 13° to 19°, or the radius of the contact area at this point is from 0.23 to 0.33 times the radius of the drop. The angle ϕ is measured from the axis of symmetry to the boundary of the contact zone. Using high-speed photography, Rochester and Brunton [8] determined that lateral outflow initiated at a critical angle $\phi = 11°$ at an impact velocity of 100 m sec^{-1}. They found that the value of ϕ did not vary for drop diameters ranging from 2 to 9 mm. It is to be noted in the experiments of Brunton and Camus [5] and Rochester and Brunton [8] that the drop is a disc of liquid generally 5 mm diameter and 1.5 mm thick. The relation between the observations for a disc-shaped drop with lateral constraint and a spherical drop remains to be established. Rochester and Brunton suggest that lateral outflow is observed at $\phi = 11^\circ$, since this is the angle at which the outward edge velocity between the drop and solid falls below the maximum possible jet velocity. Until this condition occurs the liquid cannot escape from under the drop.

Huang [17] has provided a plausible explanation for the discrepancy between the predicted and observed values of ϕ. His description of spherical drop impingement involves a three-stage impact process: the centre stamping zone, the annular digging zone, and the free jetting zone. The first stage, the centre stamping zone, is equivalent to that assumed by Bowden and Field [3] but with internal radial flow already occurring within the drop. At the first contact of the drop with the solid the maximum contact pressure is not reached instantaneously due to the compressibility of the fluid, but begins to build up toward the maximum pressure as the contact time increases. Pressure build-up initiates in the liquid in the drop at a slightly later time corresponding to the expansion of the contact area between the drop and the plane surface. This time difference due to the curvature of the drop creates radial pressure gradients which, in turn, produce internal radial flow. The angle at which the compression wave front in the liquid just overtakes the expanding boundary of the contact area is designated the critical angle, ϕ_{1c}. This is the condition for the lateral outflow used by Morris [15], Heymann [16], and Bowden and Field [3] in their analyses. As the compressional wave front overtakes the interfacial perimeter, lateral jetting begins. However, at this point with the initiation of the annular digging stage, the lateral jetting velocity is still not sufficient to overtake the velocity of the expanding contact area. The second critical angle, ϕ_{2c}, is the value of the contact angle at which the velocity of lateral jetting overtakes the velocity of the expanding contact area which is decreasing as the contact time increases. It is this second critical angle which is observed in the high speed photographic studies, as the free jetting stage begins.

On the other hand, Rochester and Brunton [8] agree with Huang's analysis for the centre stamping zone but describe different conditions in the zone of constrained lateral flow when $\phi_{1c} < \phi \leq \phi_{2c}$. Since the compression wave in the fluid is able to reach a point on the free surface of the drop before that point is overtaken by the expanding contact perimeter, a release wave is generated which propagates back into the liquid in the drop. The compression wave and attached release wave propagate along the curved wall of the drop altering its sphericity to some extent. According to Rochester and Brunton the release waves will not reduce the pressure along the axis of the drop which is still increasing. This pressure will not decrease until the edge pressure is reduced by the onset of lateral outflow which occurs when the two release waves (for the disc-shaped drop) intersect at the centre of impact.

Based on the available experimental evidence and analyses, it will be assumed that the lateral outflow is not significant for spherical drops impacting at 92 to 342 m sec^{-1} until the critical contact angle, ϕ_{2c}, falls in the range $10^\circ \leq \phi_{2c} \leq 25^\circ$. Using an idealized liquid drop model of a compressible drop striking a rigid plane, the contact radii for this condition are listed in Table I. Equation 1 is then used to compute the approximate time after initial contact at which lateral outflow would take place.

Huang's results [11] also indicate that the ratio of the lateral jetting velocity to the impact velocity decreases as the impact velocity increases. This same effect is evident in the photographic study of Jenkins and Booker [1] where 2 to $2\frac{1}{2}$ mm drops were impacted on a steel surface over a velocity range of 92 to 1140 m sec^{-1}. A plot of lateral velocity as a function of the impact velocity shows that the ratio of the velocity of lateral outflow to the velocity of impact is approximately 6 at an impact velocity of 92 m sec^{-1} while it is only 2.4 at 762 m sec^{-1}. Fyall's [4] measurement of radial outflow for a 2 mm drop striking a plate of polymethylmethacrylate at approximately 290 m sec^{-1} resulted in roughly the same ratio between the radial outflow and the normal impact velocity as found by Jenkins and Booker.

Brunton and Camus [5] have also provided photographic evidence of cavitation bubbles within an impacting drop. Cavitation bubbles were found at the liquid/solid interface during the early stage

TABLE I Critical contact radii and elapsed times for liquid drop impacts on rigid surfaces

	Drop diameter (mm)		
	0.5	1.8	2.5
Volume (mm^3)	0.654	3.05	8.19
Mass ratio	1	4.66	12.50
Maximum contact radius (mm)			
$\phi = 10^\circ$	0.0434	0.156	0.217
$\phi = 15^\circ$	0.0646	0.233	0.324
$\phi = 20^\circ$	0.0855	0.308	0.427
$\phi = 25^\circ$	0.1058	0.380	0.529
Time (μsec) required to reach maximum contact radius when $V_0 = 92\,\mathrm{m\,sec^{-1}}$			
$\phi = 10^\circ$	0.041	0.148	0.206
$\phi = 15^\circ$	0.0914	0.330	0.459
$\phi = 20^\circ$	0.160	0.576	0.799
$\phi = 25^\circ$	0.244	0.879	1.22
$V_0 = 222\,\mathrm{m\,sec^{-1}}$			
$\phi = 10^\circ$	0.0169	0.0609	0.0848
$\phi = 15^\circ$	0.0376	0.1358	0.189
$\phi = 20^\circ$	0.0658	0.237	0.330
$\phi = 25^\circ$	0.1008	0.361	0.503
$V_0 = 342\,\mathrm{m\,sec^{-1}}$			
$\phi = 10^\circ$	0.0112	0.0402	0.056
$\phi = 15^\circ$	0.0248	0.0896	0.125
$\phi = 20^\circ$	0.0435	0.157	0.218
$\phi = 25^\circ$	0.0665	0.239	0.332

of impact due to a negative pressure which results from the expansion of the compressed liquid when sideways flow begins. Brunton and Camus explain that the expanding liquid overshoots and a negative pressure forms at the surface propagating into the liquid as a tension tail to the main compression wave. Cavitation bubbles were also found to form near the rear face of the impacting drop due to the reflection of the impact pressure wave from the rear surface of the drop. The occurrence of cavitation bubbles in this region was originally suggested by Engel [14] and subsequently supported by the numerical calculations of Huang [11] and Hwang [12]. On the other hand, the photographic studies conducted by Fyall [4] for a 2 mm water drop impacting a plate of polymethylmethacrylate at 290 m sec^{-1} did not exhibit this effect. Fyall hypothesized that the pressure wave may be attenuated within the drop.

The above summarizes some of the current work on the mechanics of water drop impacts on plane surfaces. The nature of the pressure distribution which develops at a solid surface impacted by a water drop will now be considered.

For impact velocities below 300 m sec^{-1} Heymann's analysis [16] predicts a maximum pressure of approximately $3\rho_0 C_0 V_0$ which occurs at the periphery of the contact area between the drop and a rigid surface where ρ_0, C_0, V_0 are the density, acoustic velocity, and impact velocity of the liquid drop. A paraboloidal pressure distribution is obtained by Heymann with the minimum pressure occurring along the axis of spherical drop passing through the point of contact.

Huang's numerical approach [11] indicates that a hemispherical pressure distribution predominates during the very early stages of the collision. The maximum value of the pressure is reached under these conditions. As compression of the drop continues, the distribution becomes more uniform with a very slight increase in the magnitude of the pressure at the periphery of the contact area. The magnitude of the maximum value in the pressure distribution decreases as lateral outflow becomes more dominant. Huang's numerical results indicate that the maximum pressure does not exceed $0.8\,\rho_0 C_0 V_0$ for a 2 mm water drop impacting at 300 m sec^{-1}.

On the other hand, Hwang's results for a 2 mm water drop impacting a rigid plane at 300 m sec^{-1} show that the pressure rapidly rises to a value of $0.7\,\rho_0 C_0 V_0$. The pressure distribution is spatially uniform with the peak pressure occurring along the axis of symmetry of the drop impact. As the contact radius increases, the location of the maximum pressure moves to the perimeter of the contact zone and the value of the pressure along the axis of symmetry decreases. The peak pressure is found to be $1.06\,\rho_0 C_0 V_0$ and occurs at a contact radius of $0.5R$, although the results from the numerical computations for contact radii ranging from 0.5 to $0.8R$ show a sizeable degree of scatter. It does not appear that the form of the pressure distribution stipulated by Hwang can be unequivocally supported on the basis of the numerical results he presents.

Hwang also investigated the impact of a spherical water drop on an aluminium and PMMA half-space. He finds for PMMA that owing to the small deformations calculated at the liquid/solid interface, there is no appreciable difference between the drop-shape profiles for a spherical drop striking the elastic half-space and the collision with a rigid surface. Hwang also found for the same impact conditions the liquid/solid interfacial pressure on elastically deformable materials was lower and more uniform than for a rigid body. Both of these factors tend to support the simplified modelling approach to be presented in the next section.

Based on the limited time steps reported by Kreyenhagen [13], the interfacial pressure has a maximum value at the perimeter of the contact zone in the very early stages of the collision and becomes more uniform toward the later stages of the impact, after lateral outflow is initiated. These calculations show a high degree of compatability with Huang's results in other aspects of the mechanics of the collision process, except that they display a nearly instantaneous rise to the water hammer pressure which is not found to be the case for the results obtained from the numerical evaluation of Huang [11] and Hwang [12].

Using microtransducers, Rochester and Brunton [8] were able to obtain the spatial distribution of direct and shear surface stresses when a solid surface impacts a disc-shaped water drop 5 mm diameter and 1.5 mm thick. The shear stresses for smooth surfaces are negligible with respect to the magnitude of the applied pressure. The peak pressure. is approximately $1.8\,\rho_0 C_0 V_0$ and occurs at the edge of the impact area where $\phi = \phi_{2c}$, corresponding to $r/R = 0.2$. Rochester and Brunton comment on the high edge pressures. For $\phi_{1c} < \phi < \phi_{2c}$, a particle in the front surface of the drop is stopped by direct contact with the solid surface, the rate of change of momentum for such a collision will be higher than for a similar particle for which $\phi > \phi_{2c}$. For $\phi > \phi_{2c}$, the particle is separated from the solid by intervening jets carrying liquid from the centre of the drop. Accordingly, the rate of change of momentum for this particle is reduced and it does not come into direct contact with the solid.

Using strain gauges similar experimental results were obtained by Johnson and Vickers [9] who found that the maximum pressure for a cylindrical jet impacting a solid surface was $0.67\,\rho_0 C_0 V_0$ along the axis of symmetry and increased to $1.5\,\rho_0 C_0 V_0$ at the periphery of the jet. However, these results for a 50 mm jet diameter impacting an aluminium plate at $46\,\mathrm{m\,sec^{-1}}$ also indicated that shear stresses of the order of $0.45\,\rho_0 C_0 V_0$ exist near the periphery of the jet diameter, which is not consistent with the results of Rochester and Brunton cited above. Kinslow [10], on the other hand, used microtransducers to evaluate the normal peak pressure distribution for a 7.5 mm diameter jet impacting at $638\,\mathrm{m\,sec^{-1}}$. He found that the maximum pressure was $0.915\,\rho_0 C_0 V_0$ and occurred at the centre of the impact region which is consistent with the predictions of Huang. The pressure measurements were made in 1 mm increments, whereas Rochester and Brunton [8] were able to use 0.25 mm increments.

The review in this section shows that the sequence of events associated with a liquid drop striking a deformable surface at subsonic to low supersonic velocities is still a matter of speculation. In view of the level of uncertainity which prevails concerning the quantitative evaluation of the liquid/solid interfacial pressures generated, it is appropriate to investigate the response of the target materials to an idealized loading condition which may have to be modified after more definitive results for liquid drop impingement have been achieved. For the moment, the damage initiation process in the target material can be studied in terms of the idealized drop impingement model corresponding to Equation 1, as outlined in the next section.

3. Idealized model of impact event

Blowers [18] investigated the propagation of stress waves in an elastic half-space subjected to a uniform pressure, p, distributed over an expanding circular region on its surface whose time-dependent radius is deduced from the idealized model of a compressible liquid drop given in Equation 1 where

$$a(t) = [2RV_0t-(V_0t)^2]^{1/2} \approx \sqrt{(2RV_0)}\,t^{1/2} = kt^{1/2}. \tag{2}$$

The radius of the contact area, $a(t)$, increases with time according to the relation in Equation 1 which was subsequently described by Engel [19]. The pressure distribution on the surface of the solid used by Blowers in his analysis is of the form

$$\begin{aligned} p(r,t) &= p \text{ for } r \leq kt^{1/2} \\ &= 0 \text{ for } r > kt^{1/2}. \end{aligned} \tag{3}$$

The magnitude of p is assumed to be a known quantity which has to be prescribed.

While a uniform pressure distribution over the expanding contact area may not accurately represent the actual temporal development for a liquid drop impact, a uniform pressure does provide a first approximation to the actual distribution. This approach is supported in part by Hwang's numerical calculations which indicate that the pressure distribution is relatively uniform during the early stages of a liquid drop impact on a deformable half-space as opposed to a rigid half-space.

The numerical evaluation of Blower's analytical solution of the liquid drop impact problem computes the transient stress distribution within the elastic half-space in terms of the four non-vanishing stress components, the principal normal stresses, and the principal shear stresses in cylindrical coordinates. Some results from this analysis will be described for the evaluation of critical stress conditions within an elastic half-space.

Although the exact spatial and temporal distribution of the pressure over the contact zone, $p(r, t)$ in Equation 3 is not known, the one-dimensional shock wave relations for water striking a deformable substrate will provide general order of magnitude approximations to p. The balance of momentum equations are

$$p_w = \rho_w U_w (V_0 - V_w) \tag{4}$$

and

$$p_s = \rho_s U_s V_s \tag{5}$$

The water drop strikes the target with an impact velocity V_0. A shock wave is transmitted into the drop at a velocity U_w, and a second shock wave is propagated into the substrate at a velocity U_s across the water/substrate interface. The particle velocities and densities of the water and substrate are denoted by V_w, V_s and ρ_w, ρ_s, respectively. Continuity of the pressures and particle velocities at the water/substrate interface requires $p_s = p_w$ and $V_s = V_w$. Setting $V_s = V_w$ in the relation $p_s = p_w$ yields

$$V_w = \frac{V_0}{1 + (\rho_s U_s / \rho_w U_w)}. \tag{6}$$

The relation between the shock velocity and particle velocity is known for water. When the shock velocity as a function of the particle velocity is known for the substrate, Equation 6 can be solved for V_w. Then, using either Equation 4 or 5, the pressure at the water/substrate interface can be determined.

$$p_w = \frac{\rho_w U_w V_0}{1 + (\rho_w U_w / \rho_s U_s)}. \tag{7}$$

When the water drop impact velocity is small in comparison to the acoustic velocities of water and the substrate, Equation 7 reduces to

$$p_w = \frac{\rho_w C_w V_0}{1 + (\rho_w C_w / \rho_s C_s)}. \tag{8}$$

where C_w and C_s are the acoustic velocities for water and the substrate.

The variation in the shock velocity for water as a function of the particle velocity has been tabulated by Rice and Walsh [20]. The expression

$$U_w = C_0 + 2V_w - 0.1 \left(\frac{V_w}{C_0} \right) V_w \tag{9}$$

was derived by Huang [11] to approximate the relation they provided. The shock data for water will be used subsequently to evaluate the pressure applied to selected target materials by an impacting water drop.

The accuracy of the approximation used by Blowers corresponding to a compressible drop striking a rigid plane given in Equation 2 will be evaluated. The general relation can be rewritten

$$t^2 - \frac{2R}{V_0} t + \left(\frac{a}{V_0} \right)^2 = 0 \tag{10}$$

which yields

$$\frac{V_0 t}{R} = 1 - \sqrt{\left[1 - \left(\frac{a}{R} \right)^2 \right]}. \tag{11}$$

On the other hand, Blower's approximation becomes

$$\frac{V_0 t}{R} = \frac{1}{2} \left(\frac{a}{R} \right)^2. \tag{12}$$

For comparison, Equations 11 and 12 are plotted in Fig. 1. It is seen that the approximation in Equation 2 is a good representation of the exact relation for values of (a/R) less than 0.5. Equation 3 will, therefore, be applicable to the largest contact radii listed in Table I for which it is believed lateral outflow will occur.

The velocity of the expanding circular boundary defined by Equation 2 is initially supersonic but decreases as $t^{-1/2}$. The disturbance experienced by the solid medium will then be due to the propagation of a dilatation wave travelling at a velocity, C_1, the propagation of a distortional, or shear,

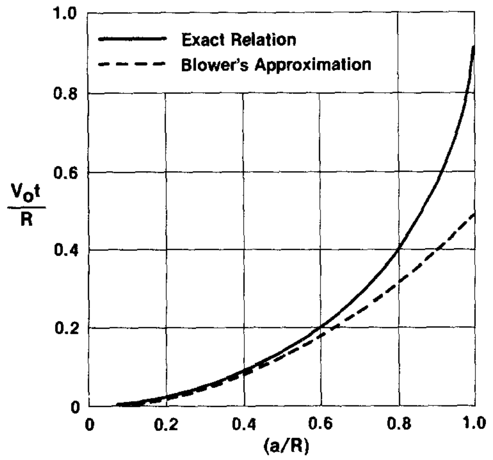

Figure 1 Comparison of the exact and approximate relations describing the rate of expansion of the contract area for a compressible drop striking a rigid plane.

wave travelling at a velocity, C_2, and a Rayleigh wave propagating along the surface at a velocity C_R which is slightly less than C_2. As long as the boundary of the loaded region is moving at a velocity $\dot{a}(t) \geq C_1$, the radius of the disturbance will be the same as that of the loaded area. When $\dot{a}(t) < C_1$, the disturbance will move ahead of the load and will continue to travel at the sonic velocity of the medium. The time at which $\dot{a}(t) = C_1$ can be determined from Equation 2

$$\tau_1 = \left(\frac{k}{2C_1}\right)^2. \tag{13}$$

Correspondingly, the shear wave will move ahead of the loaded region when

$$\tau_2 = \left(\frac{k}{2C_2}\right)^2 \tag{14}$$

where

$$C_1^2 = \left(\frac{E}{\rho}\right)\left(\frac{1-\nu}{(1+\nu)(1-2\nu)}\right) \tag{15}$$

$$C_2^2 = \left(\frac{E}{\rho}\right)\left(\frac{1}{2(1+\nu)}\right) \tag{16}$$

where E is Young's modulus, ν is Poisson's ratio, and ρ is the density of the medium.

The deformation of a spherical water drop striking rigid and elastically deformable surfaces have been computed by a few investigators. It is interesting to compare the results from these numerical computations with the idealized model in Equation 2 of the impact event for the stress wave computations. Hwang's computations [12] are based on inviscid compressible liquid. The shape of a 2 mm drop striking a rigid surface at 300 m sec^{-1} is shown in Fig. 2a: the dashed lines indicate the shape corresponding to a perfectly compressible drop impacting a rigid surface. The shape profiles from Kreyenhagen's numerical solution [13] for a 1 mm drop impacting at 205 m sec^{-1} are shown in Fig. 2b and again the corresponding profiles for a perfectly compressible drop are indicated by the dashed curves. The comparison with both numerical procedures suggest that incompressibility effects are not significant for $a/R \leq 0.5$ which includes the contact radii listed in Table I to be used in the stress wave computations, so the transient stress distributions reported here should be indicative of the very early stages of the water drop collision.

The shape history for the drop impact shown in Fig. 2b seems to indicate a more rapid expansion of the contact area than that corresponding to Hwang's computations or the idealized model. The relative magnitude of the liquid/solid interfacial pressure computed by Kreyenhagen during the initial stages of the impact is also found to be considerably lower than the values reported by Hwang.

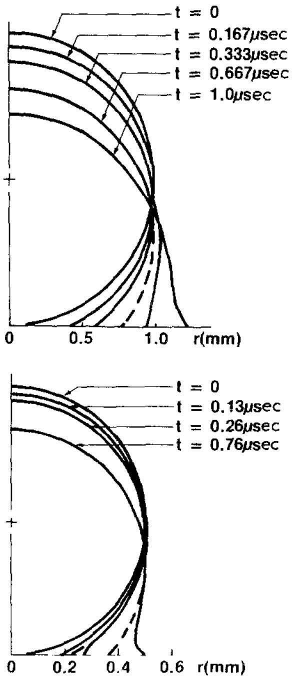

Figure 2 Computed temporal profiles of water drops striking a rigid plane. (a) 2 mm water drop impacting at 300 m sec^{-1}; (b) 1 mm water drop impacting at 205 m sec^{-1}.

Limited numerical results are provided in Blowers' paper for the case when Poisson's ratio $\nu = 0.3$. Blowers shows that the transient radial and azimuthal surface stresses at time $t = 8\tau_1$ are primarily compressive with extremely high tensile stresses found only in a narrow band immediately behind the Rayleigh wave front. Blowers comments that although extreme radial tensions arise, the radial dimensions in which they occur are always quite small. Thus, each point experiences the critical tension for an extremely short duration. Blowers conjectures that this result of the analysis tends to raise doubt in the effectiveness of the Rayleigh wave as the cause of liquid impact erosion damage. The stress states associated with the Rayleigh wave have been proposed by Bowden and Field [3] as initiating fracture in glass specimens impacted by a water jet at 600 m sec^{-1}.

More extensive computations, to be described shortly, using Blowers' analysis indicate that this conclusion regarding the duration of critical tensile stresses may have been premature. These computations indicate that there are locations in the interior of the half-space where significant tensile stresses develop for a reasonable length of time in relation to the duration of the impact event. The stresses associated with a 1.8 mm water drop striking zinc selenide, polymethylmethacrylate, and soda lime glass at 222 m sec^{-1} are computed to cover a range of material response and subsequently to compare the results from these computations with the actual damage observed on these materials. In addition, numerical computations were carried out for the range of drop diameters and velocities listed in Table I for a half-space having the elastic properties of zinc selenide.

The numerical solutions for Blowers' equations provide the stresses at all points within the elastic half-space except in the vicinity of the Rayleigh surface wave at and near the surface where a non-removable singularity in the equations prevails. Many attempts were made to overcome this difficulty in the numerical computations, but without success. The computed results reported here are given at locations within a few microns below the surface of the half-space where the calculated stresses are reasonably well-behaved including the regions in the vicinity of the Rayleigh wave front.

4. Computed stress distribution within an elastic half-space

Individual water drop imprints have been found on some of the materials tested in the AFML/Bell erosion facility. The best examples are shown in Figs. 3 and 4 for polysulphone and polymethymethacrylate (PMMA) for a 1.8 mm drop diameter impacting at 222 m sec^{-1}. Although the form of

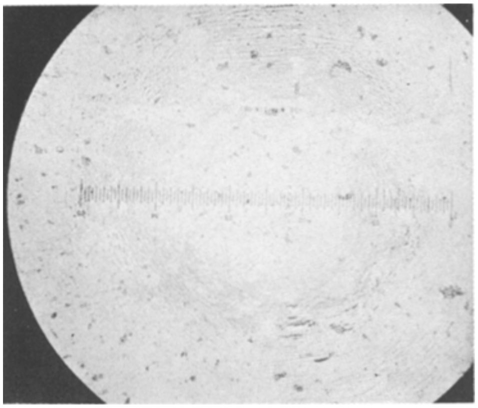

Figure 4 Imprint on the surface of polymethylmethacrylate due to a single 1.8 mm water drop impacting at 222 m sec^{-1}.

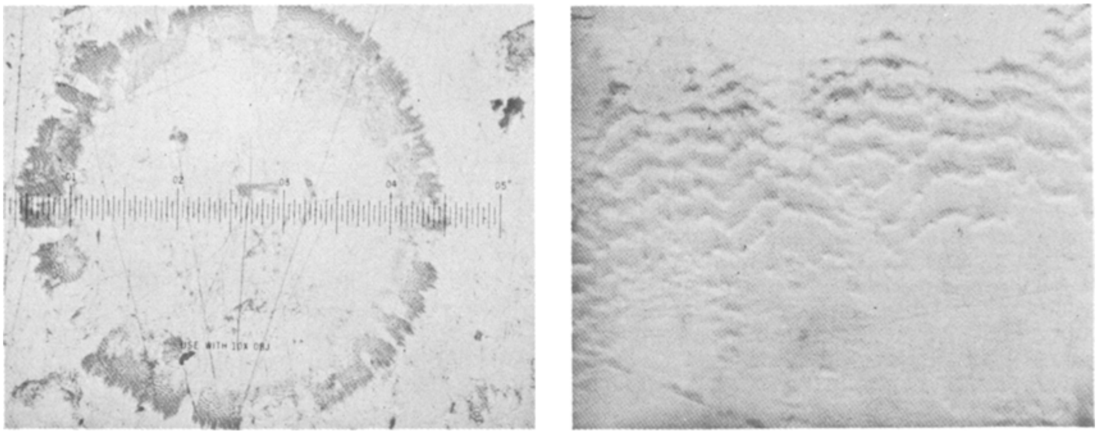

Figure 3 Multiple ripple formation of polysulphone due to a single 1.8 mm water drop impacting at 222 m sec^{-1}.

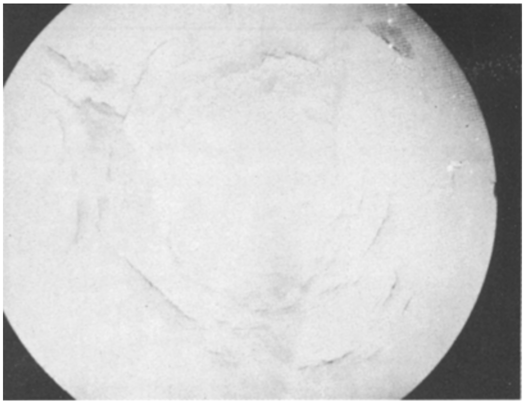

Figure 5 Ring crack formation on zinc sulphide due to 1.8 mm water drops impacting at 222 m $\sec^{-1}$.

the damage surrounding a central undamaged zone is different in the case of polysulphone and PMMA, the general features of the damage correspond to those found by other investigators at higher impact velocities. The central undamaged area for each material is approximately 0.34 to 0.38 mm radius which is only attained at the larger contact angles for the maximum contact radii listed in Table I. The cause of the damage is still a matter of speculation. Polysulphone displays a high degree of ductility when exposed to the strain-rates imposed during water drop impacts, while PMMA behaves in a semi-brittle manner under these conditions.

Zinc selenide and zinc sulphide also show a definite tendency for moderately well-defined ring fracture formations which appear to be due to a single liquid drop impact as the example in Fig. 5 illustrates. On the other hand, glasses tested at the same velocity with the exception of arsenic trisulphide, showed little tendency for ring fracture formations. The general erosive response of selected polymeric materials, glasses, and zinc sulphide and selenide is summarized in Table II for water drop impacts at 222 m $\sec^{-1}$.

The observed circular damage formations can be more readily analysed than the random forms of damage which are a more common occurrence in most of the materials investigated. Conjectures will be made regarding the sequence of events associated with the collision of a water drop with a deformable surface based on the individual drop imprints found on PMMA, polysulphone, and zinc selenide. The transient stresses calculated from Blowers' analytical solution for a compressible drop striking an elastic half-space will be used to interpret the origin of the erosion damage observed in PMMA, zinc selenide, and soda-lime glass. The material properties required in the computer evaluations of the governing equations are listed in Table III. The wave velocities are computed from the elastic moduli and densities shown using Equations 15 and 16 for the long wavelength evalu-

TABLE II Summary of erosion behaviour of transparent materials exposed to standard rainfield at 222 m $\sec^{-1}$

Zinc sulphide, zinc selenide	Initial impacts produce multiple ring fractures. Subsequent impacts extend the fracture surfaces into the interior of the bulk material with minor disruption of the exposed surface of the specimen. Complex patterns of internal fractures develop with relatively little mass loss.
Soda-lime glass, borosilicate glass	No coherent ring fractures observed in soda-lime glass but some tendency for ring fracture formations displayed in borosilicate glass. Generally random internal fracture surfaces result after numerous water drops have impacted a small region of the exposed surface. Internal fractures once initiated grow and interact to produce highly preferential removal of material from the specimen's surface.
Polymethylmethacrylate	Initial impacts produce multiple ring fractures. These fractures are very shallow in PMMA which behaves in a brittle manner. Fine-scale particle removal occurs shortly thereafter through ring fracture intersection and ring fracture interactions with surface scratches. Fairly uniform rate of material removal takes place over the entire area of the exposed surface as the exposure time increases.
Polysulphone, polycarbonate	Complete and partial multiple ring formations are observed in polysulphone; only short segments of ring formations are seen in polycarbonate. Roughening of the surface layer of the exposed surface occurs after it receives repetitive impacts due to ripple pattern intersections. Pit initiation takes place mainly at surface scratches although it subsequently occurs in highly deformed regions. Material response is ductile with evidence of permanent deformations at the rims of pits. Fracture surfaces originating at scratches penetrate the interior of the specimen and interact at favorably orientated surface scratches. Material removal is initiated by an undermining and upheaval mechanism at these sites.

TABLE III Dilatational and shear wave speeds for window materials

	Polymethylmethacrylate		Poly-sulphone	Zinc selenide	Zinc sulphide	Soda-lime glass
	Quasistatic values	High frequency data	Quasistatic values			
Specific gravity	1.19	1.184	1.24	5.27	4.08	2.47
Young's modulus (MPa $\times 10^4$)	0.31	0.90	0.25	6.71	7.44	7.0
Poisson's ratio	0.35	0.325	0.37	0.3	0.3	0.22
Dilatational wave speed C_1 (mm μsec^{-1})	2.05	2.76	1.885	4.15	4.96	5.71
Shear wave speed C_2 (mm μsec^{-1})	0.985	1.41	0.855	2.22	2.60	3.43

TABLE IV Location of shear and dilatational wave fronts (1.8 mm drop at 222 m sec^{-1} on plane $z = 0$)

Material	Maximum angle for lateral flow, ϕ	Loaded area (mm)	Shear wave front (mm)	Dilatational wave front (mm)
PMMA	10°	0.156	0.157	0.204
	15°	0.233	0.262	0.411
	20°	0.308	0.406	0.691
	25°	0.380	0.721	1.033
Zinc selenide	10°	0.156	0.181	0.277
	15°	0.233	0.347	0.588
	20°	0.308	0.572	1.008
	25°	0.380	0.847	1.522
Soda-lime glass	10°	0.156	0.238	0.365
	15°	0.233	0.495	0.793
	20°	0.308	0.842	1.371
	25°	0.380	1.267	2.079

ation except for PMMA for which high frequency experimental values are listed. The calculated values for PMMA are significantly different from the experimental values due to the viscoelastic nature of PMMA and the frequency-dependence of the viscoelastic moduli. Excluding polysulphone, the other materials listed in Table III should behave elastically.

Zinc selenide, PMMA and soda-lime glass will be subjected to the impact of a single 1.8 mm water drop at 222 m sec^{-1} in order to relate the stress wave computations to the available experimental data. The radial locations of the shear and dilatational wave fronts are provided in Table IV when the contact radii reach values corresponding to included angles ranging from 10° to 25° as recorded in Table I. The nature of the stress distributions in the three materials selected will be investigated for the larger contact angles.

4.1. Soda-lime glass

The magnitude of the stress components are normalized to unity in all of the plots which will be described. The magnitude of the actual stress component is found by multiplying the value on the graph by the magnitude of the liquid/solid interfacial pressure. Using the calculated dilatational wave velocity for soda-lime glass in Table III, Equation 6 becomes

$$V_{\mathrm{w}} = \frac{V_0}{1 + (\rho_{\mathrm{s}} C_{\mathrm{s}}/\rho_{\mathrm{w}} U_{\mathrm{w}})}. \tag{17}$$

For $V_0 = 0.222$ mm μsec^{-1}, $V_{\mathrm{w}} = 0.020$ mm μsec^{-1} and $p_{\mathrm{w}} = 302$ MPa as determined from Equation 7.

Brittle materials will be susceptible to fracture initiation in domains where tensile stresses of sufficient magnitude occur. Figs. 6 to 8 provide an overview of the regions within the half-space where tensile stresses do exist in the soda-lime target at a water drop impact velocity of 222 m sec^{-1}. These general distributions of tensile radial and normal stresses when $\phi = 15°, 20°$ and $25°$ (corresponding to Table I) indicate the dominant radial tensile stresses are only found near the surface of the specimen slightly ahead of the shear wave front

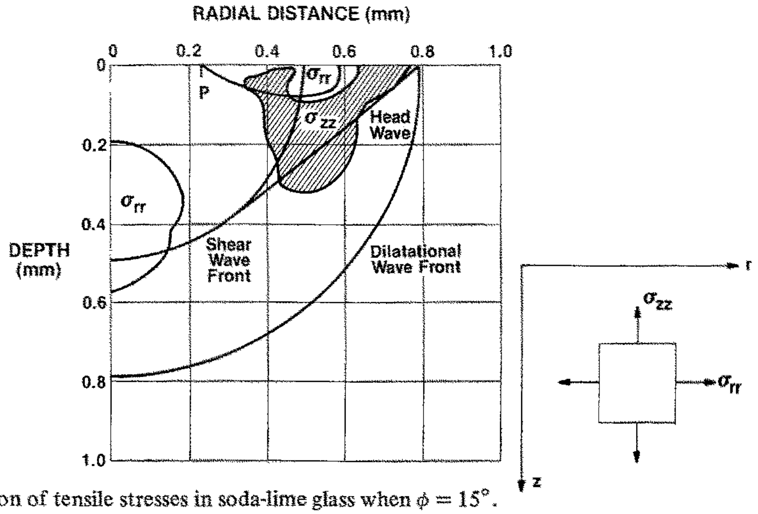

Figure 6 Distribution of tensile stresses in soda-lime glass when $\phi = 15°$.

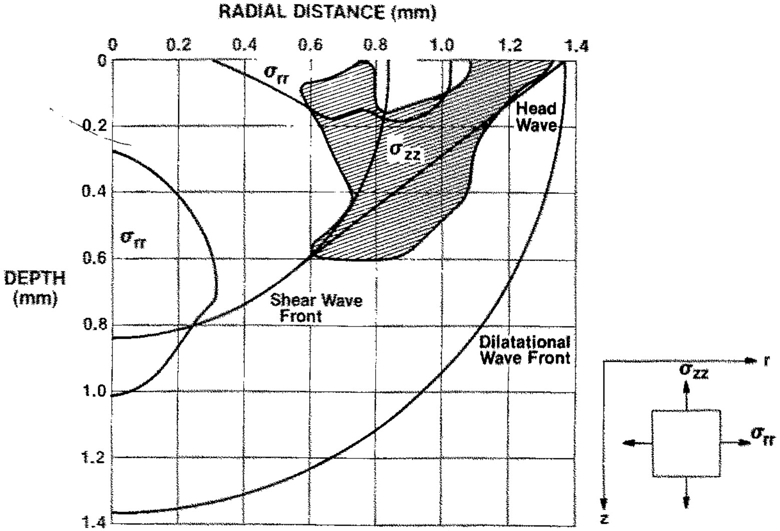

Figure 7 Distribution of tensile stresses in soda-lime glass when $\phi = 20°$.

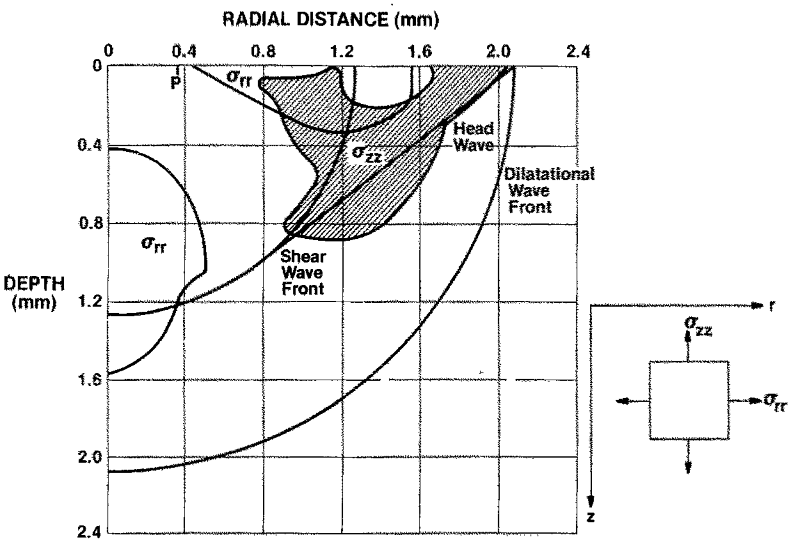

Figure 8 Distribution of tensile stresses in soda-lime glass when $\phi = 25°$.

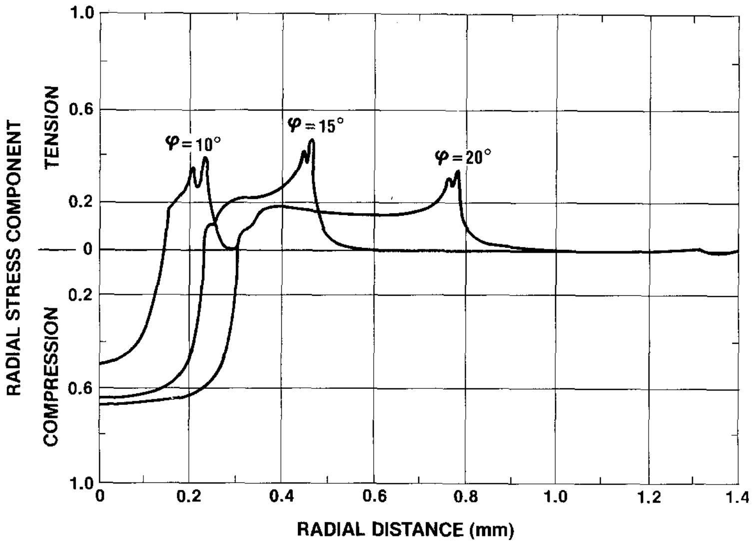

Figure 9 Variation of radial stress component in soda-lime glass with critical contact angle at $z = 10\,\mu$m.

and extending back to the loaded area. Another region of tensile radial stress exists in the vicinity of the axis through the point of initial contact between the drop and the target; however, the maximum magnitude of these stresses in on the order of 7 MPa. A fairly extensive domain wherein the normal stress components, σ_{zz}, are tensile can also be seen in these plots; however, the magnitude of these tensile stresses is quite low.

From the general maps of the stresses in a soda-lime glass target it is concluded that critical tensile stresses will generally occur at and near the surface layer at a radial distance extending from just outside the loaded region to a point slightly beyond the shear wave front. A relatively weak compressive stress is found at the surface beyond the shear wave front which is consistent with the photographic records of the impact event [4–6] and is due to the fact that the loading is normal to the plane surface of the half-space. The magnitude and extent of the radial stresses in the vicinity of the surface of the target will be considered further.

The radial stress component at $z = 10\,\mu$m for various contact angles before lateral outflow occurs is shown in Fig. 9. The temporal development of the radial stress component is shown in Fig. 10 when $\phi = 20°$. It is seen that a radial stress of approximately 50 MPa is maintained over an annulus ranging from 0.3 to 0.6 mm diameter for more than 0.1 μsec. A series of plots for the

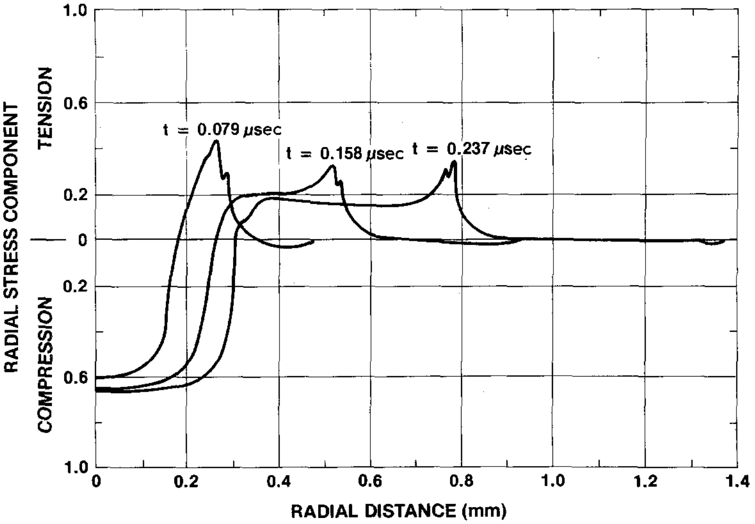

Figure 10 Temporal development of radial stress component in soda-lime glass at $z = 10\,\mu$m when $\phi = 20°$.

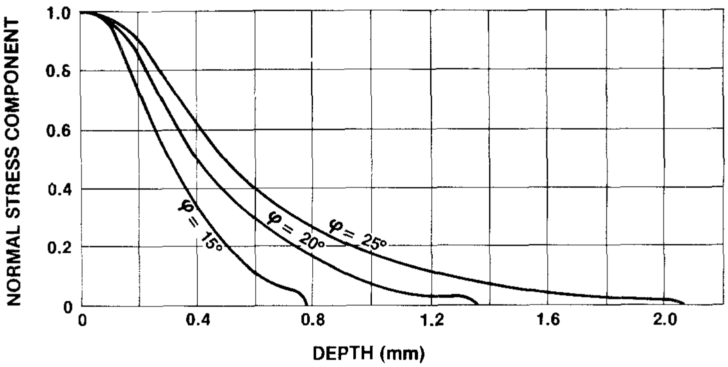

Figure 11 Variation of normal stress component (at $r = 0$) with depth in soda-lime glass.

appropriate range of r, z and t can be used to construct a fairly accurate representation of the state of stress a particular location in the half-space experiences and the time duration over which a critical stress state may prevail. The information generated in this way can be correlated with dynamic fracture mechanics analyses to estimate the extent of crack growth.

A strong compression pulse is propagated along the axis of symmetry which diminishes in intensity in the radial direction as the included angle between the axis of symmetry and the line drawn from the point of impact to a point in the half-space increases. The magnitude of the normal compressive stress, σ_{zz}, as a function of distance into the target is shown in Fig. 11 along the axis passing through the initial point of contact. In contrast to the one-dimensional shock and plane elastic wave analyses, the magnitude of this stress component decreases with distance due to the geometric attenuation of a spherical wave.

The variation in the response of the target when the elastic properties and density are changed will be illustrated for the case of polymethylmethacrylate and zinc selenide. The primary wave speeds for PMMA are lower than those for zinc selenide which, in turn, are lower than those for soda-lime glass. This difference directly affects the development of the transient stress states in these materials.

4.2. Polymethylmethacrylate

The mechanical response of PMMA is more complex than that associated with linearly elastic materials to which Blowers' analysis is applicable. The moduli for polymeric materials are a function of the frequency of the applied loadings; therefore, the long wavelength approximation to the acoustic velocities using quasistatic loading conditions are not representative of the material response for impact loadings. The acoustic velocities for PMMA have been measured in the 6 to 30 MHz frequency range [21] and will be used in the analysis which follows.

Experimental one-dimensional shock wave studies indicate that PMMA behaves as a non-linear viscoelastic material below a peak stress around 700 MPa [22]. Plastic deformations may occur at applied pressures above 700 MPa. An estimate of the magnitude of the interfacial pressure for a water drop impacting a solid surface at 0.222 mm μsec^{-1} can be determined from Equations 6 and 7, since the shock wave velocity as a function of particle velocity is known for both water and PMMA [23]. Equation 6 can be solved to yield $V_w = 0.069\ \text{mm}\ \mu\text{sec}^{-1}$ and from Equation 7 $p = 242$ MPa. Thus it is seen that plastic deformations are not to be expected under the specified impact conditions.

Although PMMA does not behave as a linear elastic solid, the transient stress distributions due to a liquid drop impact will be evaluated on this basis. The magnitude of the applied pressure will again be normalized to unity, so the actual magnitude of the stresses can be determined by whatever procedure is used to evaluate the pressure at the water/solid interface.

Radial tensile stresses in PMMA only occur in a very shallow layer near the free surface of the target for 1.8 mm drops impacting at 222 m sec^{-1}. The form of the radial stress for a range of values of ϕ is shown in Fig. 12 at a depth of 10 μm. The decrease in the magnitude of the radial stress component with depth is indicated in Fig. 13 while the temporal development of the radial stress compo-

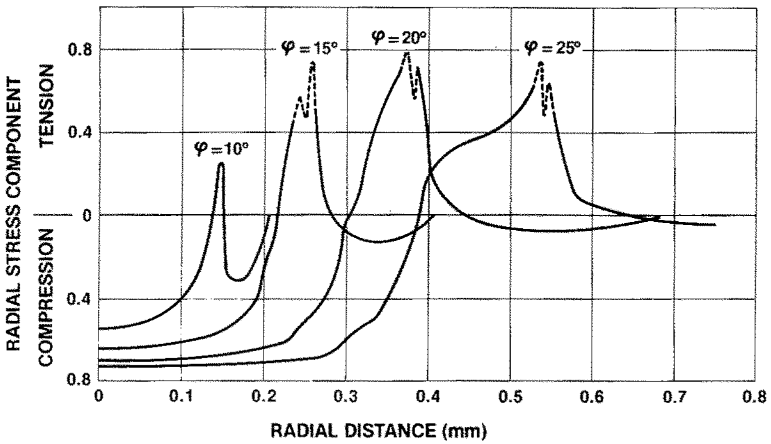

Figure 12 Variation of radial stress component in PMMA with critical contact angle at $z = 10\,\mu m$.

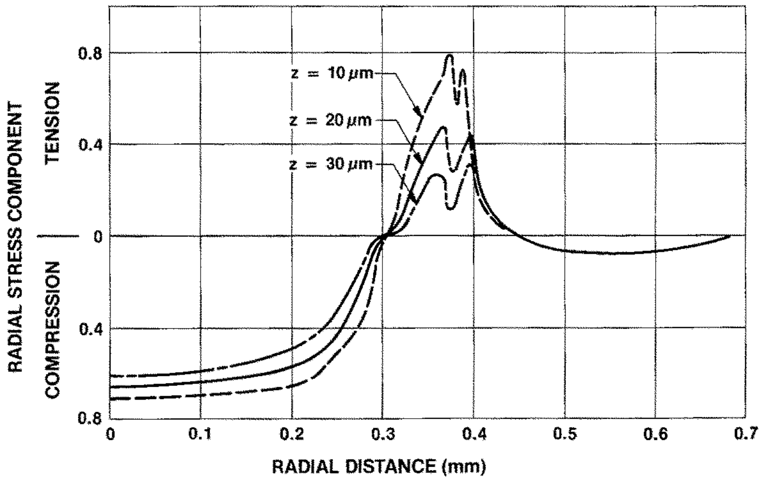

Figure 13 Variation of radial stress component in PMMA with depth when $\phi = 20°$.

nent is shown in Figs. 14 and 15. The attenuation of the compressive normal pressure pulse with distance into the specimen is shown in Fig. 16.

The level of sustained radial stress for a 1.8 mm water drop striking PMMA at $222\,\mathrm{m\,sec^{-1}}$ when $\phi = 25°$ is approximately 75 MPa according to Fig. 12 and from 50 to 125 MPa when $\phi = 20°$ using Fig. 14. The comparison with the corresponding curves for soda-lime glass is striking. The magnitude of the tensile stresses for PMMA is considerably larger than for soda-lime glass, and the radial dimension over which it is applied is about four times less. It might be expected, therefore, that the localized nature of the loading will produce correspondingly localized deformations of the target.

4.3. Zinc selenide

Using the calculated dilatational wave velocity for zinc selenide in Table III, Equation 17 yields $V_w = 0.013\,\mathrm{mm\,\mu sec^{-1}}$ when $V_0 = 222\,\mathrm{m\,sec^{-1}}$. Then $p_w = 312\,\mathrm{MPa}$ as determined from Equation 7. The magnitude of the liquid/solid interfacial pressure for an impact velocity of $342\,\mathrm{m\,sec^{-1}}$ is 485 MPa.

The magnitude of the radial stresses in the critical region near the surface surrounding the point of impact is indicated in Figs. 17 and 18 for a water drop impact of 222 and $342\,\mathrm{m\,sec^{-1}}$, respectively. The graphs shown are for one instant of time when the loaded area reaches an included angle of $\phi = 25°$. The magnitude of the tensile stresses can be compared for 0.5, 1.8, and 2.5 mm

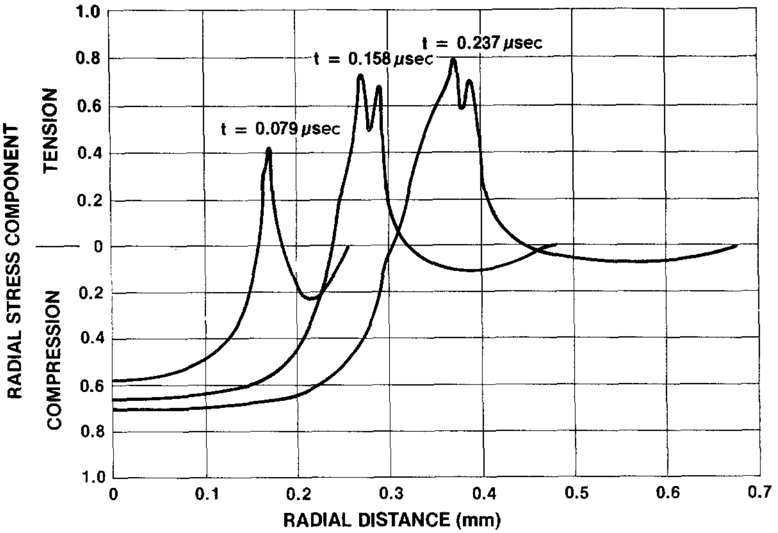

Figure 14 Temporal development of radial stress component in PMMA at $z = 10\,\mu m$ when $\phi = 20°$.

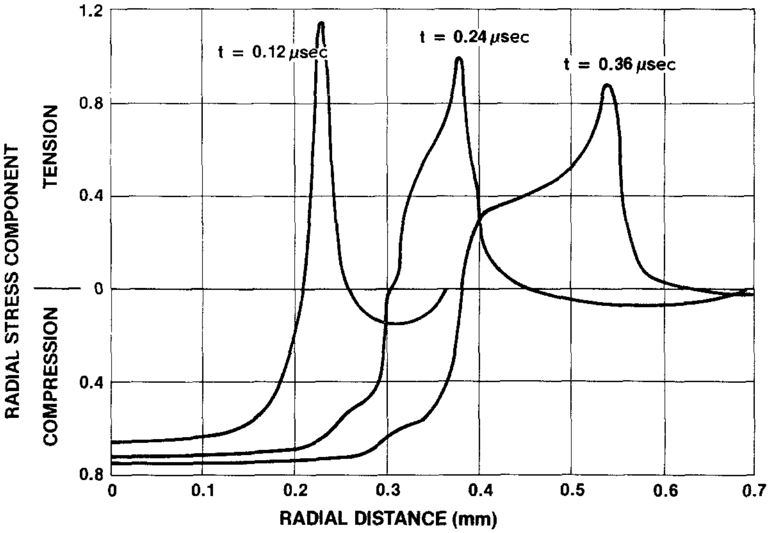

Figure 15 Temporal development of radial stress component in PMMA at $z = 5\,\mu m$ when $\phi = 25°$.

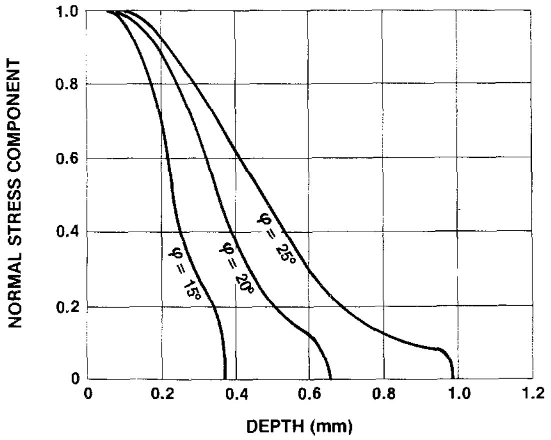

Figure 16 Variation of normal stress component (at $r = 0$) with depth in PMMA.

drop diameters. It is seen that at this time the duration of the tensile stress for an 0.5 mm water drop is exceedingly short. The direct effects of this size drop at higher velocities would probably be detrimental, but fracture initiation through stress wave interactions with existing flaws does not seem very probable for the short pulse durations imposed on the target. The durations and magnitude of the transient tensile stresses for the 1.8 and 2.5 mm drops do seem capable of producing the circumferential fractures observed on the surface of zinc selenide specimens. The magnitude of the tensile stresses are comparable for the 1.8 and 2.5 mm drops; however, the duration of these stress levels is longer for the 2.5 mm drop, and

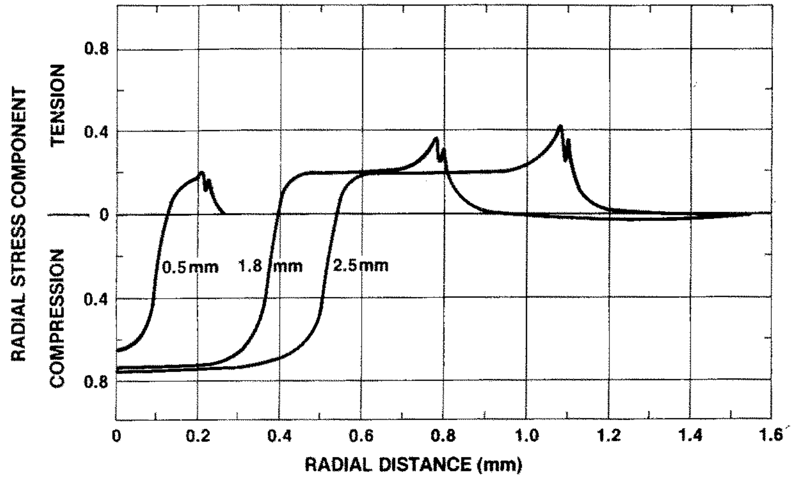

Figure 17 Variation of radial stress component (at $z = 10\,\mu\text{m}$) with drop diameter for impacts at $222\,\text{m}\,\text{sec}^{-1}$ on ZnSe ($\phi = 25°$).

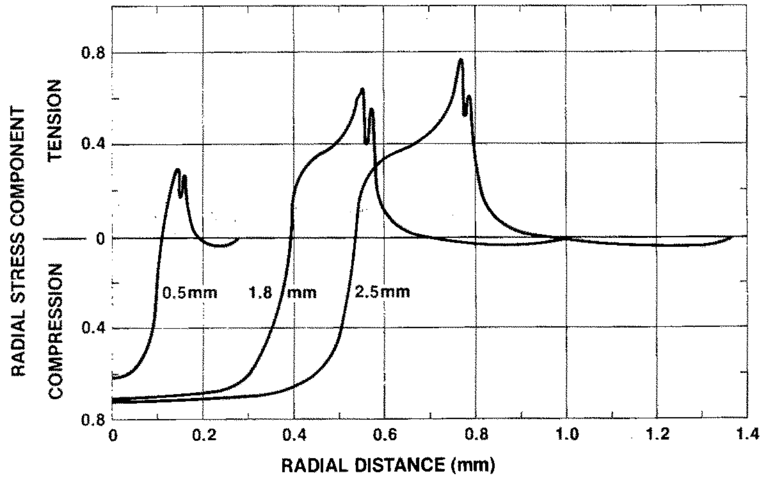

Figure 18 Variation of radial stress component (at $z = 10\,\mu\text{m}$) with drop diameter for impacts at $342\,\text{m}\,\text{sec}^{-1}$ on ZnSe ($\phi = 25°$).

correspondingly the resulting damage should be more extensive. From these graphs at $z = 10\,\mu\text{m}$ the sustained tensile radial stress $\sigma_{rr} = 60\,\text{MPa}$ at $V_0 = 222\,\text{m}\,\text{sec}^{-1}$. At $342\,\text{m}\,\text{sec}^{-1}$ σ_{rr} is maintained at a value exceeding 175 MPa for a reasonably long duration with respect to the impact event. The magnitude of the sustained tensile radial stress at $V_0 = 222\,\text{m}\,\text{sec}^{-1}$ is comparable to that for PMMA, however, the time duration the tensile stress is maintained is almost four times longer for zinc selenide.

The temporal development of the stress states prior to lateral outflow when $\phi = 25°$ for a 1.8 mm water drop is shown in Fig. 19. The variation of this stress with depth into the target is indicated in Fig. 20.

All of the plots of the stresses for the three materials considered and a variety of impact conditions are presented to illustrate the general nature of the transient stress distributions within the target. Such plots are moderately easy to compute and can now be used to investigate the onset of crack initiation for a range of materials and particle impact conditions.

5. Discussion

One explanation for the circular damage formations in Figs. 3 and 4 would be that the undamaged region is depressed during the period preceding lateral outflow and tensile bending stresses develop outside the depressed region [4, 24]. The material within an annulus surrounding the central region

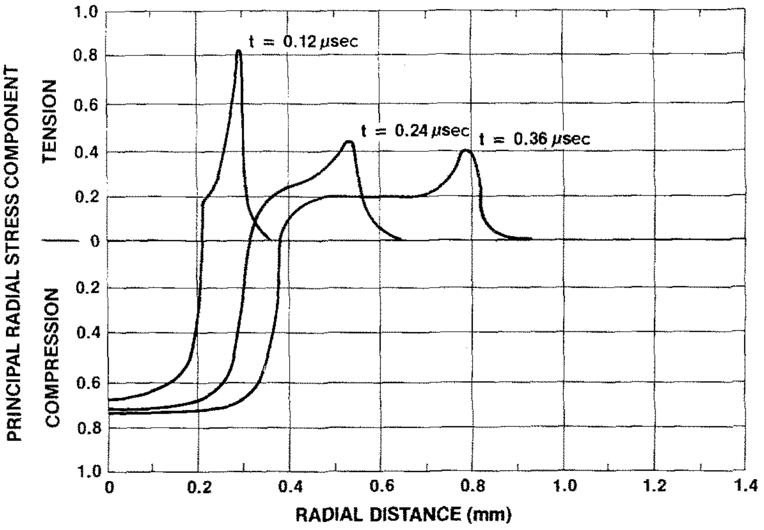

Figure 19 Temporal development of principal radial stress component in ZnSe at $z = 10\,\mu\text{m}$ when $\phi = 25°$ for a 1.8 mm drop impacting at $222\ \text{m sec}^{-1}$.

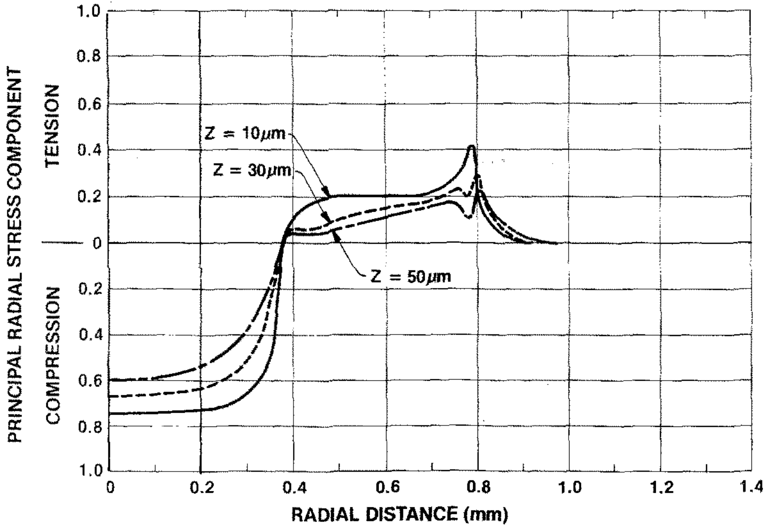

Figure 20 Variation of principal radial stress component in zinc selenide with depth for 1.8 mm drop impacting at $222\ \text{m sec}^{-1}$ ($\phi = 25°$).

is then stressed beyond the yield point and after the applied pressure subsides, localized wrinkling can occur within this annulus. This would account for the ripple pattern shown in Fig. 3 for polysulphone but no large-scale permanent deformations are found within the compressed zone. The magnitude of the applied pressure has to be such that the compressive stresses which develop within the central undamaged region are not sufficient to yield the material in this region, but the magnitude of the deformations surrounding the central region are sufficient to produce local yielding of the material in tension. The same reasoning can be applied to polymethylmethacrylate. However, due to the semibrittle nature of this material, microcracks occur in the region surrounding the depressed zone in order to accommodate the tensile field which develops during the drop impact.

An alternative line or reasoning would ascribe the circular damage zones to stress wave phenomena. The computed dilatational wave velocity, C_1, and shear wave velocity, C_2, for the polymers as well as the corresponding values for zinc selenide, zinc sulphide and soda-lime glass are listed in Table III. The stress wave computations indicate that the critical tensile stresses occur after the shear wave has propagated outward from the contact area. The location of the shear wave fronts for the

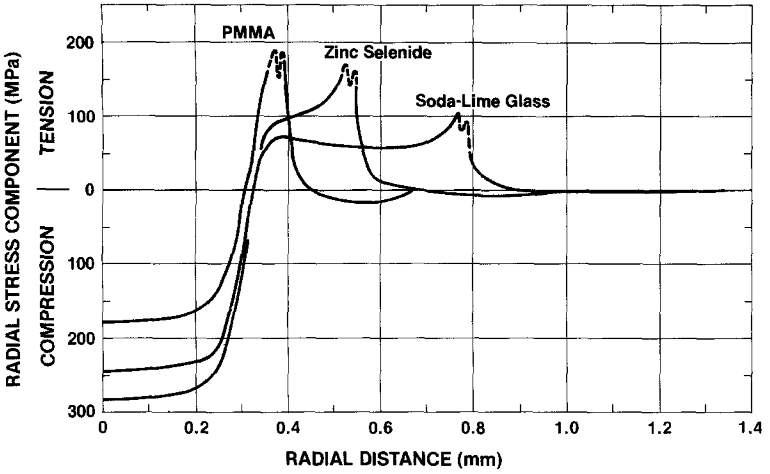

Figure 21 Variation of radial stress component at $z = 10\,\mu m$ for 1.8 mm water drop impacting various materials at 222 $m\,sec^{-1}$ ($\phi = 20°$).

contact radii considered in the numerical computations are listed in Table IV. The actual radial stress distributions for PMMA, zinc selenide, and soda-lime glass are shown in Fig. 21 when $\phi = 20°$. The comparison indicates that although the intensity of the applied pressure is the least for PMMA the radial stresses at this instant of time are more confined and more intense than for the other two materials. The depression mechanism described earlier, therefore, seems to be supported by these calculations in the case of polymethylmethacrylate and polysulphone. On the other hand, the composition of the transient waves will be fully established in the annular region around the impact zone to which each material responds in its own way. The magnitude of the tensile stress decreases more rapidly in soda-lime glass as compared to zinc selenide due to the higher wave speeds in soda-lime glass.

The actual magnitude of the normal stress component as a function of depth into the target is shown in Fig. 22 for PMMA, zinc selenide and soda-lime glass. For the normal stress component the higher wave velocity for soda-lime glass tends to maintain the magnitude of the stress at a higher level to a greater depth than for the other materials represented.

The comparison between the computed and experimental results appears to be consistent: the magnitude and duration of the transient tensile stresses at and near the surface must be sufficient to initiate crack growth at a number of locations around the central point of contact. The interaction of subsequent drop impacts with a system of small fractures on the surface is still not completely evident. Once a series of small cracks are present on the surface it is difficult to isolate the stress wave effects generated by a drop impact in the vicinity of these flaws and crack propagation which takes place due to the direct pressure applied to a pre-existing crack. Details of the microscopic observations of the fracture behaviour of transparent materials will be described in subsequent papers; however, much remains to be learned about the correlation of fracture data with the transient stress distributions in the target materials [25].

On the basis of both the experimental and numerical results it would seem that the analytical

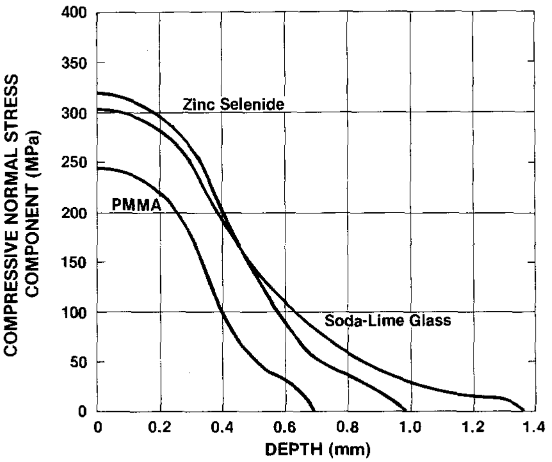

Figure 22 Variation of normal stress component (at $r = 0$) with depth for 1.8 mm water drop impacting various materials at 222 $m\,sec^{-1}$ ($\phi = 20°$).

approach developed here is a viable approach for understanding the transient stresses generated in an elastic body during the period when the direct pressure applied to the surface by the impacting drop dominates the collision. While some difficulties are encountered in evaluating the stresses at the plane surface of the half-space in the analytical approach, the stress values can be prescribed throughout the half-space and show a consistent variation from point to point. The finite difference schemes, on the other hand, display a fairly high level of irregularity in the results presented to date due to the requirement that a reasonable grid size be used in order to maintain economical computer times. It is important to note that consideration of the elastic properties alone is not sufficient to differentiate the range of the response displayed by materials under dynamic loadings. Additional material characterization is required if a correlation between the material properties and erosion damage is to be developed as will become evident in the publications which follow to describe the erosion of PMMA, ZnSe and inorganic glasses.

Acknowledgements

This work was funded under Air Force Contract F33615-73-C-5057. The research was carried out while the author was employed by Bell Aerospace Company Division of Textron, Buffalo, New York. The co-operation and assistance of the Air Force Materials Laboratory Project Monitors, G. F. Schmitt and T. L. Peterson, is gratefully acknowledged. The author would like to thank R. M. Blowers of the Central Electricity Research Laboratories, Leatherhead, Surrey, UK, for providing a listing of the TURBAN computer program which is the basis for evaluating the transient stresses in an elastic half-space. The author also appreciates the diligence of Ms Alice Drobot, formerly affiliated with the Computer Center at Bell Aerospace Company, who modified and made the TURBAN program operational.

References

1. D. C. JENKINS and J. D. BOOKER, The Impingement of Water Drops on a Surface Moving at High Speed, in "Aerodynamic Capture of Particles", edited by E. G. Richardson (Pergamon Press, New York, 1960).
2. F. P. BOWDEN and J. H. BRUNTON, *Proc. Roy. Soc. (London)* **A263** (1961) 433.
3. F. P. BOWDEN and J. E. FIELD, *ibid* **A282** (1964) 331.
4. A. A. FYALL, "Single Impact Studies with Liquids and Solids", in Proceedings of the Second Conference on Rain Erosion, Meersburg, West Germany (August 1967).
5. J. H. BRUNTON and J. J. CAMUS, "The Flow of a Liquid Drop During Impact" in Proceedings of the Third International Conference on Rain Erosion and Associated Phenomena, Elvetham Hall, Hampshire, UK (August 1970).
6. J. E. FIELD, J. J. CAMUS, D. A. GORHAM and D. G. RICKERBY, "Impact Damage Produced by Large Water Drops", in Proceedings of the Fourth International Conference on Rain Erosion and Associated Phenomena, Meersburg, West Germany (May 1974).
7. M. C. ROCHESTER and J. H. BRUNTON, "The Influence of the Physical Properties of the Liquid on the Erosion of Solids", in Erosion, Wear and Interfaces with Corrosion, ASTM STP 567 (December 1974).
8. M. C. ROCHESTER and J. G. BRUNTON, "Surface Pressure Distribution During Drop Impingement", in Proceedings of the Fourth International Conference on Rain Erosion and Associated Phenomena, Meersburg, West Germany (May 1974).
9. W. JOHNSON and G. W. VICKERS, *J. Mech. Eng. Sci.* **15** (1973) 302.
10. R. KINSLOW, Tennessee Technological University Report TTU-ES-74-3 (October 1974).
11. Y. C. HUANG, PhD Dissertation, University of Michigan (1971).
12. J. B. G. HWANG, PhD Dissertation, University of Michigan (1975).
13. K. N. KREYENHAGEN, personal communication.
14. O. G. ENGEL, *J. Res. Nat. Bur. Stand.* **54** (1955) 281.
15. J. W. MORRIS Jun., Mechanistic Investigation of Rain Erosion, AFML TR-69-287, Part II (September 1969).
16. F. J. HEYMANN, *J. Appl. Phys.* **40** (1969) 5113.
17. Y. C. HUANG, "Three Stage Impact Process in Liquid Impingement", in Proceedings of the Fourth International Conference on Rain Erosion and Associated Phenomena, Meersburg, West Germany (May 1974).
18. R. M. BLOWERS, *J. Inst. Math. Applics.* **5** (1969) 167.
19. O. G. ENGEL, *J. Appl. Phys.* **44** (1973) 692.
20. M. H. RICE and J. M. WALSH, *J. Chem. Phys.* **26** (1957) 824.
21. J. R. ASAY, D. L. LAMBERSON and A. H. GUENTHER, *J. Appl. Phys.* **40** (1969) 1768.
22. K. W. SCHULER, *J. Mech. Phys. Solids* **18** (1970) 277.
23. L. M. BARKER and R. E. HOLLENBACH, *J. Appl. Phys.* **41** (1970) 4208.
24. O. G. ENGEL, *J. Res. Nat. Bur. Stand.* **54** (1955) 51
25. A. G. EVANS and T. R. WILSHAW, "Dynamic Solid Particle Impacts in Brittle Materials: An Appraisal", *J. Mater. Sci.* **12** (1977) 97.

Received 28 July and accepted 20 October 1976.